Research Square

Preprints are preliminary reports that have not undergone peer review.
They should not be considered conclusive, used to inform clinical practice,
or referenced by the media as validated information.

# Relative Permeability Uncertainty in Geological $CO_2$ Storage: A Full-Cycle SCAL-Based Modeling Framework and Its Impact on Long-Term Storage Performance

**Muhammad Nur Ali Akbar**
Rock Flow Dynamics Ltd
**Bettina Jenei**
bettina.jenei@tu-clausthal.de
Technology University Clausthal
**Mark Lakos**
Rock Flow Dynamics Ltd
**Bastian Steffens**
Rock Flow Dynamics Ltd
**Serkan Kulaksiz**
Rock Flow Dynamics Ltd
**Leonhard Ganzer**
Technology University Clausthal

**Method Article**

**Keywords:** relative permeability, $CO_2$ storage, SCAL modeling, uncertainty quantification, plume migration, residual trapping, solubility trapping, saline aquifer, CCS

**Posted Date:** June 18th, 2026

**DOI:** https://doi.org/10.21203/rs.3.rs-9732211/v1

**License:** This work is licensed under a Creative Commons Attribution 4.0 International License.
Read Full License

**Additional Declarations:** No competing interests reported.

# Relative Permeability Uncertainty in Geological $CO_2$ Storage: A Full-Cycle SCAL-Based Modeling Framework and Its Impact on Long-Term Storage Performance

**M. N. A. Akbar[1,2]*, B. Jenei[2], M. Lakos[1], B. Steffens[1], S. Kulaksiz[1], and L. Ganzer[2]**

**[1]Rock Flow Dynamics Ltd, Aberdeen, United Kingdom**

**[2]Technology University Clausthal, Clausthal-Zellerfeld, Germany**

***Corresponding author: mn.aliakbar@gmail.com**

## ABSTRACT

Supercritical $CO_2$–brine relative permeability is a fundamental control on multiphase flow, plume migration, injectivity, and trapping efficiency in geological $CO_2$ storage. This study presents an integrated, full-cycle SCAL-based modeling framework that explicitly quantifies uncertainty in primary drainage and imbibition $CO_2$–brine relative permeability and systematically propagates this uncertainty into long-term dynamic reservoir simulations. The workflow combines physics-driven trend models, analogue experimental datasets, and Corey-type parameterization to generate optimistic, base-case, and pessimistic relative permeability scenarios, with all Corey parameters expressed as functions of initial water saturation ($S_{wi}$).

Primary drainage relative permeability trends were derived from 37 coreflood experiments spanning sandstone, carbonate, and basalt samples compiled from the NETL–CO2BRA database, while imbibition and residual trapping behavior were assembled from published experimental studies. The resulting uncertainty-bounded drainage and imbibition curves were implemented in a three-dimensional compositional reservoir simulation using the CO2STORE framework to evaluate $CO_2$ injectivity, plume evolution, dissolution, and trapping mechanisms over a 2-year injection period and a 1,000-year post-injection period.

Simulation results demonstrate that relative permeability uncertainty is not a secondary modeling detail but a first-order control on $CO_2$ storage performance. Optimistic scenarios, characterized by lower $CO_2$ endpoint relative permeability and higher residual gas saturation, produce compact and vertically confined plumes, enhanced residual and solubility trapping, and improved long-term containment, albeit with moderately higher injection pressures. Pessimistic scenarios favor injectivity

but result in faster plume migration, larger plume footprints, sustained mobile $CO_2$ fractions, and reduced trapping efficiency. By explicitly integrating drainage and imbibition uncertainty within a single coherent SCAL-based workflow and propagating it through dynamic simulations, this study provides a robust and transparent framework for CCS risk assessment, storage design, and project optimization under conditions of limited experimental data availability.

**Keywords:** relative permeability; $CO_2$ storage; SCAL modeling; uncertainty quantification; plume migration; residual trapping; solubility trapping; saline aquifer; CCS

## INTRODUCTION

Geological carbon dioxide ($CO_2$) storage is widely recognized as a critical technology for mitigating anthropogenic greenhouse gas emissions and enabling large-scale decarbonization of the energy sector. Among the available subsurface storage options, deep saline aquifers and depleted hydrocarbon reservoirs offer the largest global storage capacity and broad geographical distribution. The long-term success of these systems depends on the ability to reliably predict how injected $CO_2$ migrates, dissolves, and becomes immobilized in the subsurface over timescales extending well beyond the operational injection period (Bachu, 2008; Bachu and Adams, 2003; Benson and Cole, 2008).

Dynamic reservoir simulation is the primary tool used to evaluate $CO_2$ plume evolution, pressure response, and trapping behavior during both injection and post-injection phases. These simulations rely on physically consistent representations of multiphase flow between supercritical $CO_2$ and formation brine. A central input governing these processes is the $CO_2$–brine relative permeability, which determines phase mobility and regulates the balance between flow, trapping, and dissolution (Juanes et al., 2006; Class et al., 2009; Krevor et al., 2012; Wang et al., 2020 ; Akbar and Myhr, 2024). Relative permeability behavior in $CO_2$–brine systems is inherently hysteretic and strongly dependent on displacement history, with drainage and imbibition paths governed by phase connectivity, wettability, and capillary trapping mechanisms (Juanes et al., 2006; Spiteri et al., 2008). Primary drainage describes the displacement of brine by $CO_2$ during the injection phase and largely controls injectivity, plume migration, and vertical segregation under buoyancy. In contrast, imbibition describes the re-entry of brine following injection shut-in and governs residual trapping of $CO_2$ through pore-scale snap-off and ganglion formation (Spiteri et al., 2008; Pini and Benson, 2017). Figure 1 provides a conceptual overview of this hysteretic $CO_2$–brine relative permeability behavior,

illustrating the distinct drainage and imbibition paths and emphasizing the roles of irreducible water saturation, residual $CO_2$ trapping, and evolving phase connectivity in controlling plume evolution and long-term storage security. This conceptual framework highlights why drainage and imbibition behavior must be treated as coupled components when assessing $CO_2$ storage performance.

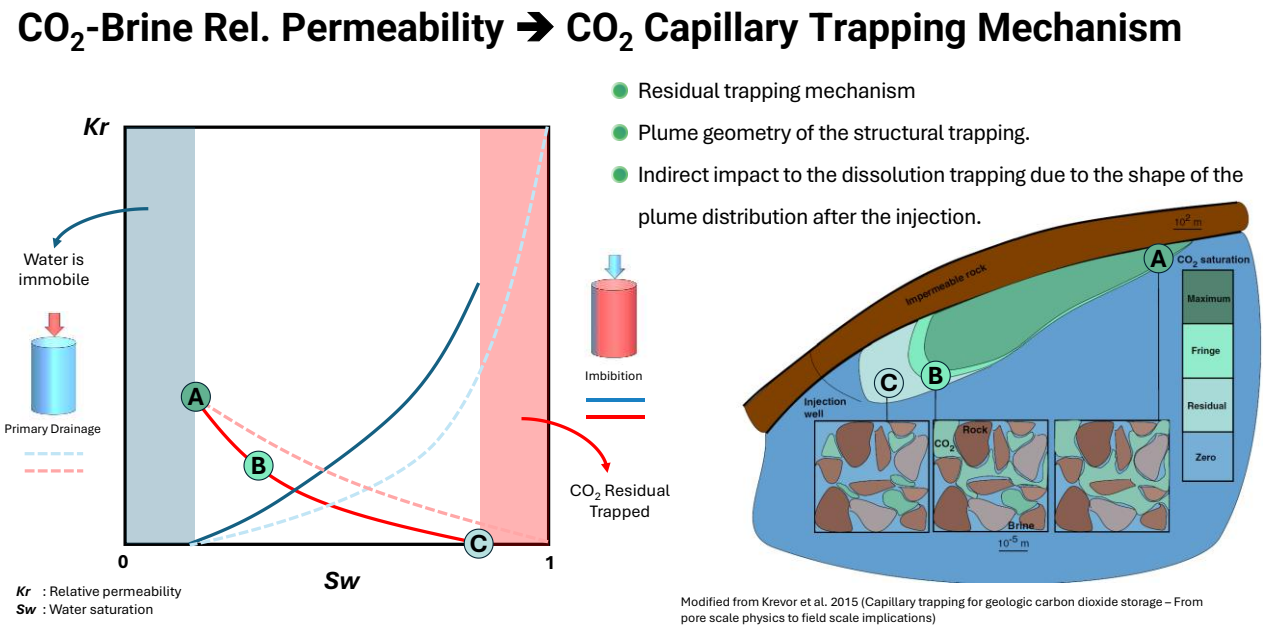



**Fig. 1** — Conceptual representation of hysteretic $CO_2$–brine relative permeability during primary drainage ($CO_2$ injection) and imbibition (post-injection brine re-entry), emphasizing the roles of irreducible water saturation, residual $CO_2$ trapping, and phase connectivity in controlling $CO_2$ plume evolution and long-term storage security. Adapted from Akbar et al. (2026) and Krevor et al. (2015).

Despite their importance, reliable special core analysis (SCAL) measurements for supercritical $CO_2$–brine systems remain limited. Laboratory experiments conducted under CCS-relevant pressures and temperatures require specialized equipment, strict safety protocols, and careful control of wettability and boundary conditions. As a result, available datasets are sparse and exhibit significant scatter across lithologies, experimental methodologies, and flow regimes (Anderson, 1986a,b; Anderson, 1987a,b; Müller, 2011; Mathias et al., 2013; Kianinejad et al., 2016). Consequently, many CCS studies rely on simplified or generic relative permeability functions, often treating them as deterministic inputs and neglecting uncertainty and hysteresis effects.

Uncertainty in relative permeability parameters—such as irreducible water saturation, endpoint relative permeabilities, residual gas saturation, and Corey exponents—translates directly into

uncertainty in predicted injectivity, plume migration, trapping efficiency, and long-term containment. Previous studies have demonstrated that these uncertainties can exert a dominant control on CCS performance, particularly during post-injection periods when residual and solubility trapping govern plume stabilization (Juanes et al., 2006; Krevor et al., 2012; Akbarabadi and Piri, 2013; Mathias et al., 2013). However, many existing assessments consider drainage and imbibition behavior in isolation, apply relative permeability deterministically, or do not consistently propagate SCAL-scale uncertainty into long-term, field-scale storage predictions.

This study addresses that gap by presenting a fully integrated, SCAL-based uncertainty modeling framework that jointly captures uncertainty in primary drainage and imbibition $CO_2$–brine relative permeability behavior and explicitly propagates this uncertainty into long-term reservoir simulations. The framework builds on recent advances in Corey-parameter trend modeling for $CO_2$–brine systems (Akbar et al., 2025), extending the methodology to cover both displacement regimes within a single coherent workflow. The resulting optimistic, base-case, and pessimistic relative permeability models are interpreted as physics-based bounding cases rather than probabilistic realizations, providing a transparent and defensible basis for CCS performance assessment under limited experimental data availability.

Specifically, the objectives of this study are to: (1) develop a physics-based and data-driven SCAL modeling workflow to generate uncertainty-bounded primary drainage and imbibition $CO_2$–brine relative permeability curves informed by analogue experimental datasets and wettability-controlled trends; (2) implement these uncertainty scenarios in dynamic compositional reservoir simulations to quantify their impact on $CO_2$ plume migration, dissolution, and trapping behavior over injection and 1,000-year post-injection periods; and (3) evaluate how critical relative permeability uncertainty modeling is for robust CCS design, risk assessment, and long-term storage security.

## DATASET

The relative permeability dataset used in this study was compiled from multiple published experimental sources to represent a broad spectrum of reservoir conditions relevant to geological $CO_2$ storage. The primary objective of assembling this dataset was to capture the variability in $CO_2$–brine multiphase flow behavior arising from differences in lithology, pore structure, wettability, and experimental conditions, providing a robust basis for SCAL-based uncertainty modeling.

***Primary Drainage Dataset***

Primary drainage relative permeability data were adopted from Akbar et al. (2025) and reconciled from coreflood experiments compiled within the NETL–$CO_2$BRA Relative Permeability Database (Crandall et al., 2019). The database was developed to systematically assemble $CO_2$–brine relative permeability measurements conducted under reservoir-relevant pressure and temperature conditions, with applications in geological $CO_2$ sequestration and enhanced oil recovery. The compiled dataset spans a wide range of sedimentary rock types and depositional environments relevant to saline aquifer storage.

Figure 2 summarizes the experimental primary drainage $CO_2$–brine relative permeability measurements for carbonate and sandstone samples, illustrating the substantial variability observed in both curve shape and endpoint behavior across lithologies and experimental conditions. The scatter evident in these measurements reflects differences in pore structure, wettability, saturation history, and experimental methodology, and underlines the inherent uncertainty associated with laboratory-derived relative permeability data for $CO_2$–brine systems.

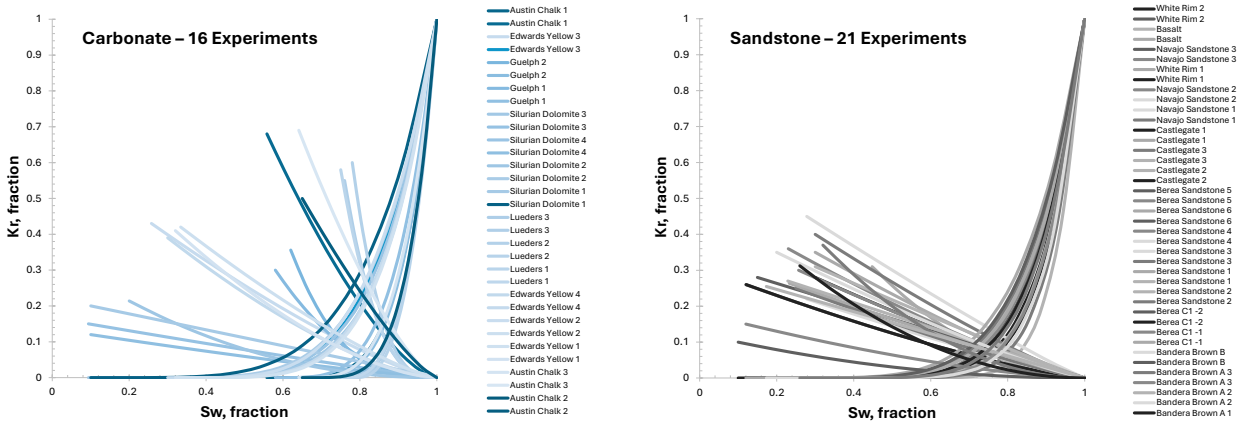



**Fig. 2** — Experimental primary drainage $CO_2$–brine relative permeability measurements for carbonate (left) and sandstone (right) samples compiled from the NETL–$CO_2$BRA analogue SCAL database, illustrating significant variability in curve shape and endpoint behavior across lithologies and experimental conditions. Reproduced from Akbar et al. (2026).

The primary drainage dataset comprises 37 unsteady-state, constant-rate coreflood experiments using supercritical $CO_2$ and brine. Sixteen experiments were conducted on carbonate samples, including limestones and dolomites from shallow-marine and reef environments, with porosities ranging from approximately 6 to 28% and permeabilities between 0.16 and 327 mD. Twenty experiments were performed on sandstone samples representing marginal marine, strand plain, barrier bar, deltaic,

fluvial, and aeolian depositional settings, with porosities of 15–26% and permeabilities between 41 and 865 mD. One additional experiment was conducted on a volcanic mafic basalt sample with a porosity of 9.1% and a permeability of 72.3 mD. Together, these data span more than three orders of magnitude in permeability and provide a robust basis for characterizing uncertainty in primary drainage $CO_2$–brine relative permeability behavior.

### *Imbibition and Residual Trapping Dataset*

Imbibition relative permeability data were assembled from previously published experimental studies reported by Bennion and Bachu (2008, 2010) and Bachu (2013). These datasets include laboratory measurements for sandstone and carbonate formations under supercritical $CO_2$–brine conditions, covering a broad range of pressures, temperatures, salinities, and permeability scales. Sandstone samples exhibit porosities of approximately 9–24% and permeabilities spanning over five orders of magnitude (from ~0.006 to 1,560 mD), while carbonate samples show porosities between about 9 and 17% with permeabilities ranging from approximately 0.02 to 370 mD. All imbibition experiments were conducted using supercritical $CO_2$–brine systems with brine salinities between 2,000 and 27,000 ppm, ensuring consistency with saline aquifer storage conditions. To further constrain capillary trapping behavior, additional residual $CO_2$ gas saturation data were incorporated from Krevor et al. (2015), providing complementary insight into pore-scale and core-scale trapping mechanisms.

## SCAL-BASED RELATIVE PERMEABILITY UNCERTAINTY MODELING

The SCAL-based modeling framework adopted in this study is designed to explicitly quantify uncertainty in $CO_2$–brine relative permeability and propagate this uncertainty into reservoir-scale simulations. Rather than relying on a single deterministic curve, the workflow generates uncertainty-bounded primary drainage and imbibition relative permeability models that are physically consistent and grounded in experimental data. This approach enables a systematic assessment of how uncertainty in multiphase flow parameters controls injectivity, plume migration, and long-term trapping behavior.

The optimistic, base-case, and pessimistic relative permeability scenarios are not intended to represent formal probabilistic percentiles (e.g., P10, P50, P90) derived from stochastic sampling. Instead, they represent physically consistent uncertainty envelopes constructed through a combination of data-driven trends derived from analogue SCAL datasets, physics-based constraints informed by wettability-controlled multiphase flow behavior, and expert judgment. This approach ensures that the

resulting uncertainty bounds honor both experimental variability and physically plausible displacement mechanisms, while avoiding assumptions of statistical completeness that are often unrealistic given the limited availability of CCS-relevant relative permeability data.

A Corey-based SCAL modeling framework was recently developed by Akbar et al. (2025a,b) for oil and gas applications. In that approach, individual SCAL experiments are parameterized by fitting endpoint saturations and curve-shape parameters, while each flow parameter is expressed as a function of initial water saturation ($S_{wi}$). These trend models, grounded in wettability and multiphase-flow physics, were calibrated against the comprehensive SCAL database (Ebeltoft et al., 2014), allowing the workflow to capture experimental scatter while maintaining physical consistency. The methodology is readily adaptable to specific fields or lithologies through recalibration of the trend parameters.

***Mathematical Formulation of Trend Parameters***

All relative permeability curves are generated using Corey-type functions (Corey, 1954). The supercritical $CO_2$ (gas) relative permeability is expressed as:

$$k_{rg} = k_{rg}^{0}(1 - S_{wn})^{ng} \tag{1}$$

and the water relative permeability as:

$$k_{rw} = k_{rw}^{0}(S_{wn})^{nw} \tag{2}$$

Where $k_{rg}^{0}$ and $k_{rw}^{0}$ are the endpoint relative permeabilities to $CO_2$ at irreducible/residual water saturation ($S_{wir}$) and to water at residual gas saturation ($S_{gr}$), respectively. *ng* and *nw* are the Corey exponents for gas and water. The normalized water saturation $S_{wn}$ is defined as:

$$S_{wn} = \frac{(S_w - S_{wir})}{(1 - S_{wir} - S_{gr})} \tag{3}$$

In this study, the irreducible water saturation ($S_{wir}$) is assumed equivalent to the initial water saturation ($S_{wi}$), such that $S_{wir} = S_{wi}$. The relationship between initial water saturation and absolute permeability is described using a power-law expression,

$$S_{wir} = S_{wi} = a(k)^{-b} \tag{4}$$

where $k$ is absolute permeability and $a$ and $b$ are calibrated constants (from this study (Figure 3a) $a$ = 0.75 and $b$ = 0.26). This relationship establishes $S_{wi}$ as a physically meaningful organizing variable that implicitly captures the effects of pore structure, capillary entry pressure, and wettability on multiphase displacement behavior.

Building on this definition, Equations (4)–(9) collectively define the SCAL trend model used to generate all primary drainage and imbibition Corey parameters as continuous and physically correlated functions of $S_{wi}$. The endpoint $CO_2$ relative permeability, Corey exponents for $CO_2$ and brine, residual gas saturation, and brine endpoint relative permeability are expressed as

$$K_{rg@Swir} = C_{K_{rg}} + \left(A_{K_{rg}} - C_{K_{rg}} + B_{K_{rg}} \times S_{wi}^{M_{Krg}}\right) \times (1 - S_{wi})^{G_{Krg}} \quad (5)$$

$$n_g = C_{ng} + \left(A_{ng} - C_{ng} + B_{ng} \times S_{wi}^{M_{ng}}\right) \times (1 - S_{wi})^{G_{ng}} \quad (6)$$

$$n_w = C_{nw} + (A_{nw} - C_{nw} + B_{nw} \times (1 - S_{wi})^{M_{nw}}) \times (S_{wi})^{W_{nw}} \quad (7)$$

$$S_{gr} = C_{S_{grw}} + \left(A_{S_{grw}} - C_{S_{grw}} + B_{S_{grw}} \times S_{wi}^{M_{Sgrw}}\right) \times (1 - S_{wi})^{G_{Sgrw}} \quad (8)$$

$$K_{rw@Sgr} = C_{K_{rw}} + \left(A_{K_{rw}} - C_{K_{rw}} + B_{K_{rw}} \times S_{wir}^{M_{Krw}}\right) \times (1 - S_{wir})^{G_{Krw}} \quad (9)$$

where the coefficients $A$, $B$, $C$, $M$, $G$, and $W$ are model constants specific to each parameter:

- $X_{Krg}$ = *Parameter in* $K_{rg@Swir}$, *X = A, B, C, M, G.*
- $X_{ng}$ = *Parameter in* $n_g$, *X = A, B, C, M, G.*
- $X_{nw}$ = *Parameter in* $n_w$, *X = A, B, C, M, W.*
- $X_{Krw}$ = *Parameter in* $K_{rw@Sgr}$, *X = A, B, C, M, G.*
- $X_{Sgr}$ = *Parameter in* $S_{gr}$, *X = A, B, C, M, G.*

The coefficients $A$, $B$, $C$, $M$, and $G/W$ appearing in Equations (5)–(9) are summarized in Table 1. These coefficients were calibrated using compiled analogue SCAL datasets under reservoir-relevant pressure and temperature conditions and constrained by wettability-controlled and physics-based

multiphase flow behavior. This combined data-driven and physics-based calibration ensures that the resulting parameter trends are physically consistent across lithologies and permeability ranges.

The SCAL trend model defined by Equations (4)–(9) forms the basis for the primary drainage and imbibition parameter relationships presented in Figures 3a–d and 4a–d, respectively. These parameter trends are subsequently propagated into full relative permeability curves for representative reservoir conditions, as illustrated in Figures 3e–f and 4e–f.

Uncertainty bounds are incorporated by applying physically consistent multipliers to the base-case parameter trends defined by Equations (4)–(9), thereby generating optimistic and pessimistic scenarios that represent bounding cases of $CO_2$–brine multiphase flow behavior. The calibrated model constants and corresponding uncertainty multipliers for all parameters are summarized in Table 1. These uncertainty-bounded trends form the basis for the primary drainage and imbibition relative permeability envelopes presented in Figures 3 and 4.

**Table 1** — Summary of SCAL model constants (A, B, C, M, G/W) and uncertainty multipliers (Opt. Mult. and Pess. Mult.) for primary drainage and imbibition relative permeability parameterization. Multipliers are applied to base-case Corey parameter curves to produce optimistic and pessimistic scenarios.

| Parameter | A | B | C | M | G/W | Opt. Mult. | Pess. Mult. |
|---|---|---|---|---|---|---|---|
| *Primary Drainage* | | | | | | | |
| $K_{rg@Swir}$ | 0.05 | 0.6 | 0.6 | 1 | 1 | 0.6 | 1.4 |
| $n_g$ | 1 | 2 | 2.5 | 1 | 1.5 | 0.6 | 1.4 |
| $n_w$ | 7 | 1 | 2 | 1 | 1.3 | 0.65 | 1.35 |
| *Imbibition* | | | | | | | |
| $K_{rw@Sgr}$ | 0.9 | 0.3 | 0 | 1 | 1.5 | 0.5 | 1.5 |
| $n_g$ | 7 | 0 | 1 | 2 | 1.5 | 0.6 | 1.4 |
| $n_w$ | 7 | 1 | 1.6 | 4 | 3 | 0.6 | 1.4 |
| $S_{gr}$ | 0.5 | 0.3 | 0 | 1 | 0.95 | 0.2 | 0.2 |

***Primary Drainage Relative Permeability Uncertainty***

Figure 3 summarizes the SCAL-based modeling of primary drainage $CO_2$–brine relative permeability and the associated uncertainty bounds, using initial (irreducible) water saturation ($S_{wi}$) as the key organizing variable. As defined by Equation (4), $S_{wi}$ reflects the combined influence of pore structure,

capillary entry pressure, and wettability, and therefore provides a physically meaningful link between rock properties and multiphase displacement behavior during $CO_2$ injection.

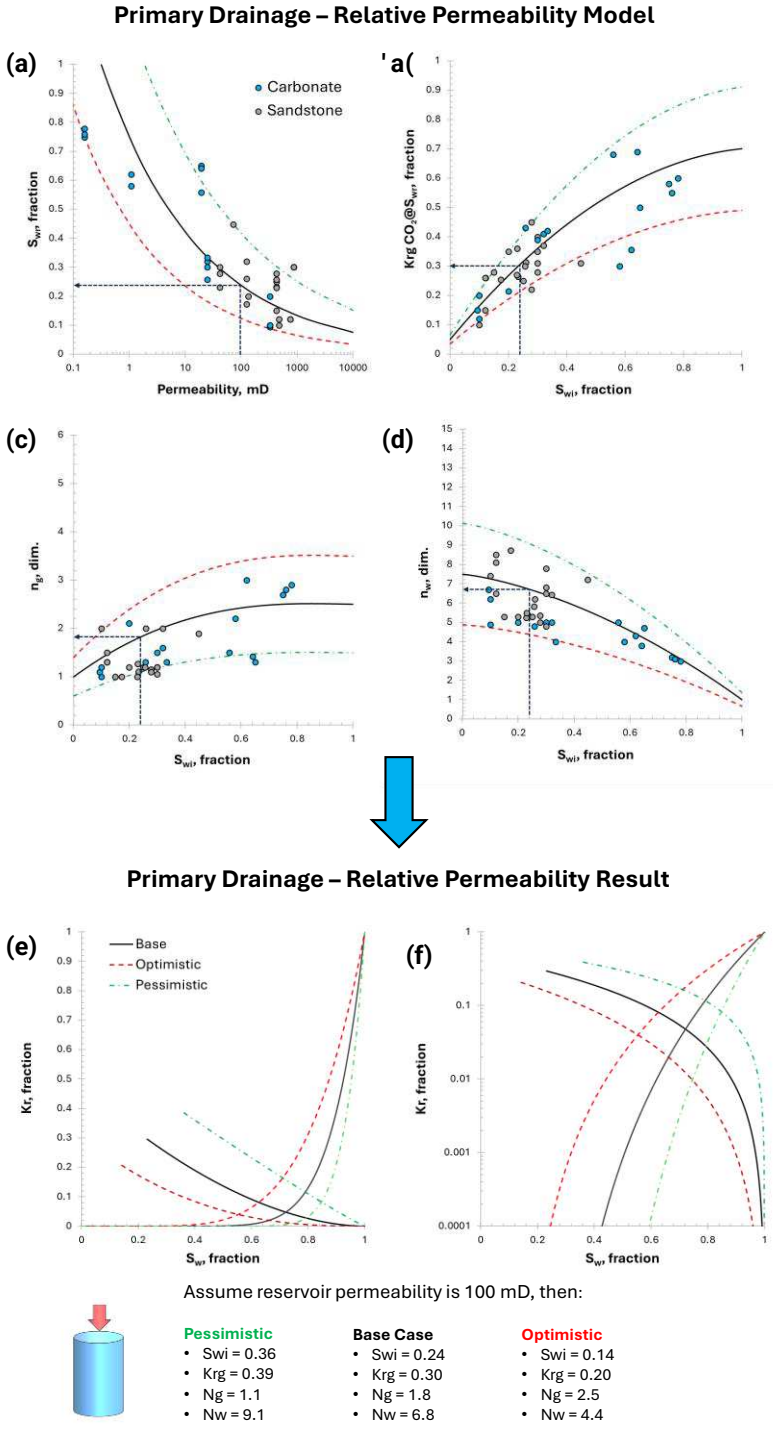



**Fig. 3** — SCAL-based primary drainage relative permeability modeling for the supercritical $CO_2$–brine system with uncertainty bounds. Subfigures show: (a) $S_{wi}$ versus absolute permeability; (b) $CO_2$

endpoint relative permeability at $S_{wi}$ ($K_{rg@Swi}$) versus $S_{wi}$; (c) $CO_2$ Corey exponent (ng) versus $S_{wi}$; (d) water Corey exponent ($n_w$) versus $S_{wi}$; (e) and (f) representative primary drainage relative permeability curves in linear and semi-log scale for a reservoir permeability of 100 mD, illustrating optimistic, base-case, and pessimistic uncertainty scenarios. Adapted from Akbar et al. (2026).

Figure 3a illustrates the inverse relationship between $S_{wi}$ and absolute permeability across carbonate and sandstone samples, whereby lower-permeability rocks retain higher irreducible water saturations as a result of stronger capillary forces associated with smaller pore throats. This relationship demonstrates that $S_{wi}$ should not be treated as an independent endpoint saturation, but rather as a proxy for drainage efficiency and pore-scale flow accessibility.

The dependence of $CO_2$ endpoint relative permeability on $S_{wi}$ (Fig. 3b) reveals a counterintuitive trend: despite lower $S_{wi}$ implying greater $CO_2$ pore occupancy, the $CO_2$ endpoint relative permeability decreases with decreasing $S_{wi}$. This behavior indicates that $CO_2$ mobility at irreducible water saturation is governed primarily by phase connectivity rather than saturation magnitude. In low-$S_{wi}$ rock samples, $CO_2$ invades smaller pores and pore throats at higher capillary pressures, resulting in more tortuous and weakly connected flow pathways.

The corresponding Corey exponent trends (Figs. 3c and 3d) further support this interpretation. The $CO_2$ Corey exponent decreases with decreasing $S_{wi}$, reflecting delayed formation of a spanning $CO_2$ flow network and connectivity-limited behavior. In contrast, the brine Corey exponent increases as $S_{wi}$ decreases, indicating stronger wetting-phase control and the persistence of continuous brine films that restrict $CO_2$ flow. Together, these trends demonstrate that $S_{wi}$ exerts a first-order control on primary drainage relative permeability through its linkage to pore structure, wettability, and displacement mechanisms.

The uncertainty envelopes shown in Figure 3 arise from physically consistent variations in Corey parameters generated by the SCAL trend model defined by Equations (4)–(9), using the coefficients and uncertainty multipliers summarized in Table 1. Applying these uncertainty bounds, representative primary drainage relative permeability curves for a reservoir permeability of 100 mD are shown in Figures 3e and 3f. In the optimistic scenario, reduced $CO_2$ endpoint relative permeability and higher brine relative permeability promote compact plume development and increased $CO_2$–brine contact during injection. In contrast, the pessimistic scenario exhibits higher $CO_2$ mobility at lower $CO_2$ saturations, favoring injectivity but accelerating plume migration and lateral plume growth. The

base-case response lies between these end-member behaviors and serves as the reference trend for subsequent analysis.

***Imbibition Relative Permeability Uncertainty***

In contrast to primary drainage, imbibition relative permeability behavior reflects the pore-scale $CO_2$ distribution established during the preceding drainage stage and is therefore inherently hysteretic. During imbibition, brine re-enters the pore space following injection shut-in, leading to $CO_2$ snap-off, ganglion formation, and progressive loss of gas-phase connectivity. As a result, imbibition behavior exerts a primary control on residual $CO_2$ trapping and long-term plume stabilization.

Figure 4 presents the SCAL-based uncertainty modeling of imbibition relative permeability using the same $S_{wi}$-based organizing framework as primary drainage, but with trends that reflect differences in phase disconnection and trapping rather than flow accessibility. Figure 4a shows the relationship between residual $CO_2$ gas saturation ($S_{gr}$) and $S_{wi}$, revealing a systematic increase in residual trapping with decreasing $S_{wi}$. This trend is consistent with the Land trapping correlation (Land, 1968), in which greater drainage during injection leads to higher maximum gas saturation and, consequently, greater residual trapping during subsequent imbibition. Rocks that experienced more extensive drainage during injection therefore contain larger volumes of disconnected $CO_2$ that are susceptible to snap-off during subsequent imbibition, resulting in more effective capillary trapping.

Figure 4b illustrates the dependence of brine endpoint relative permeability at residual gas saturation on $S_{wi}$. Higher $S_{wi}$ values are associated with lower brine endpoint permeabilities despite lower residual gas saturation, reflecting poorer pore connectivity and higher tortuosity in capillary-dominated rocks. In contrast, low-$S_{wi}$ cases preserve efficient brine flow during imbibition due to sustained wetting-phase connectivity through films and pore corners.

The Corey exponent trends for imbibition (Figs. 4c and 4d) further capture the hysteretic nature of the process. The $CO_2$ Corey exponent decreases with increasing $S_{wi}$, indicating more rapid loss of gas mobility where residual trapping is weaker. Conversely, the brine Corey exponent increases with $S_{wi}$, reflecting enhanced capillary sensitivity and increased curvature in the brine relative permeability response. These opposing trends emphasize the fundamental differences between drainage and imbibition displacement mechanisms.

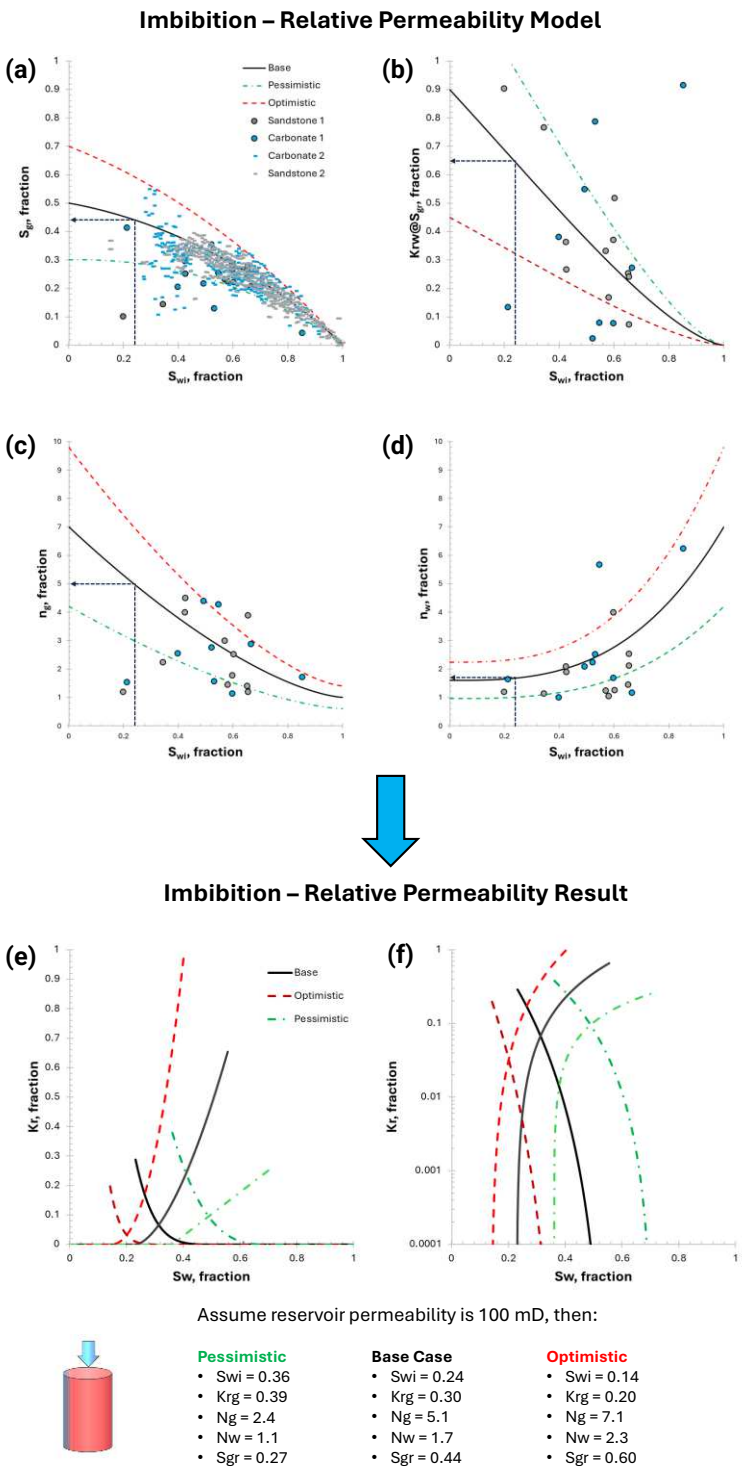



**Fig. 4** — SCAL-based imbibition relative permeability modeling for the supercritical $CO_2$–brine system with uncertainty bounds. Subfigures illustrate: (a) residual $CO_2$ gas saturation ($S_{gr}$) versus $S_{wi}$; (b) brine endpoint relative permeability at $S_{gr}$ versus $S_{wi}$; (c) $CO_2$ Corey exponent versus $S_{wi}$; (d) water Corey exponent versus $S_{wi}$; (e) and (f) representative imbibition relative permeability curves in linear and semi-log scale for a reservoir permeability of 100 mD, showing optimistic, base-case, and

pessimistic scenarios and highlighting hysteresis effects relevant to residual trapping. Adapted from Akbar et al. (2026).

The uncertainty envelopes in Figure 4 are generated using the same SCAL trend model defined by Equations (4)–(9), with physically consistent uncertainty multipliers applied to the imbibition parameters listed in Table 1. Representative imbibition relative permeability curves for a reservoir permeability of 100 mD are shown in Figures 4e and 4f. The optimistic imbibition scenario exhibits high residual $CO_2$ saturation and strong water-phase dominance, leading to rapid loss of gas mobility and efficient plume immobilization following injection shut-in. In contrast, the pessimistic scenario retains a larger mobile $CO_2$ fraction, allowing continued plume migration and delayed stabilization during the post-injection period.

***Application Across Permeability Classes/ Simplified Rock Type***

A key strength of the SCAL modeling framework presented here is its flexibility and generalizability. While the uncertainty scenarios discussed above were constructed for a representative reservoir permeability of 100 mD, the workflow is not limited to a single permeability value or rock type. By defining the irreducible (or initial) water saturation ($S_{wi}$) for any given rock group—typically derived from permeability or a flow unit classification scheme—the SCAL trend model can generate physically consistent relative permeability curves tailored to that group. This makes the framework directly applicable across the full range of reservoir heterogeneity encountered in real CCS storage sites.

To illustrate this capability, Figure 7 presents example primary drainage relative permeability curves generated for four distinct rock groups (RG-1 through RG-4), defined using a simple and practical classification based on permeability, with each group spanning approximately one logarithmic cycle. Rock group RG-1, representing very high permeability formations (~2,000 mD), exhibits the lowest $S_{wi}$ (~0.10) and correspondingly low $CO_2$ endpoint relative permeability (~0.16), reflecting efficient brine drainage but connectivity-limited $CO_2$ flow. Rock group RG-2 corresponds to high permeability formations (~200 mD), RG-3 to moderate permeability (~20 mD), and RG-4 to low permeability formations (~5 mD), with $S_{wi}$ increasing and flow behavior becoming progressively more capillary-dominated across the sequence. The intermediate rock groups RG-2 and RG-3 display transitional behavior between these end-members. This straightforward permeability-based grouping is intentionally simple, requiring only permeability as an input, and is designed to demonstrate the

minimum effort needed to apply the SCAL framework across reservoir heterogeneity in the absence of detailed rock typing data.

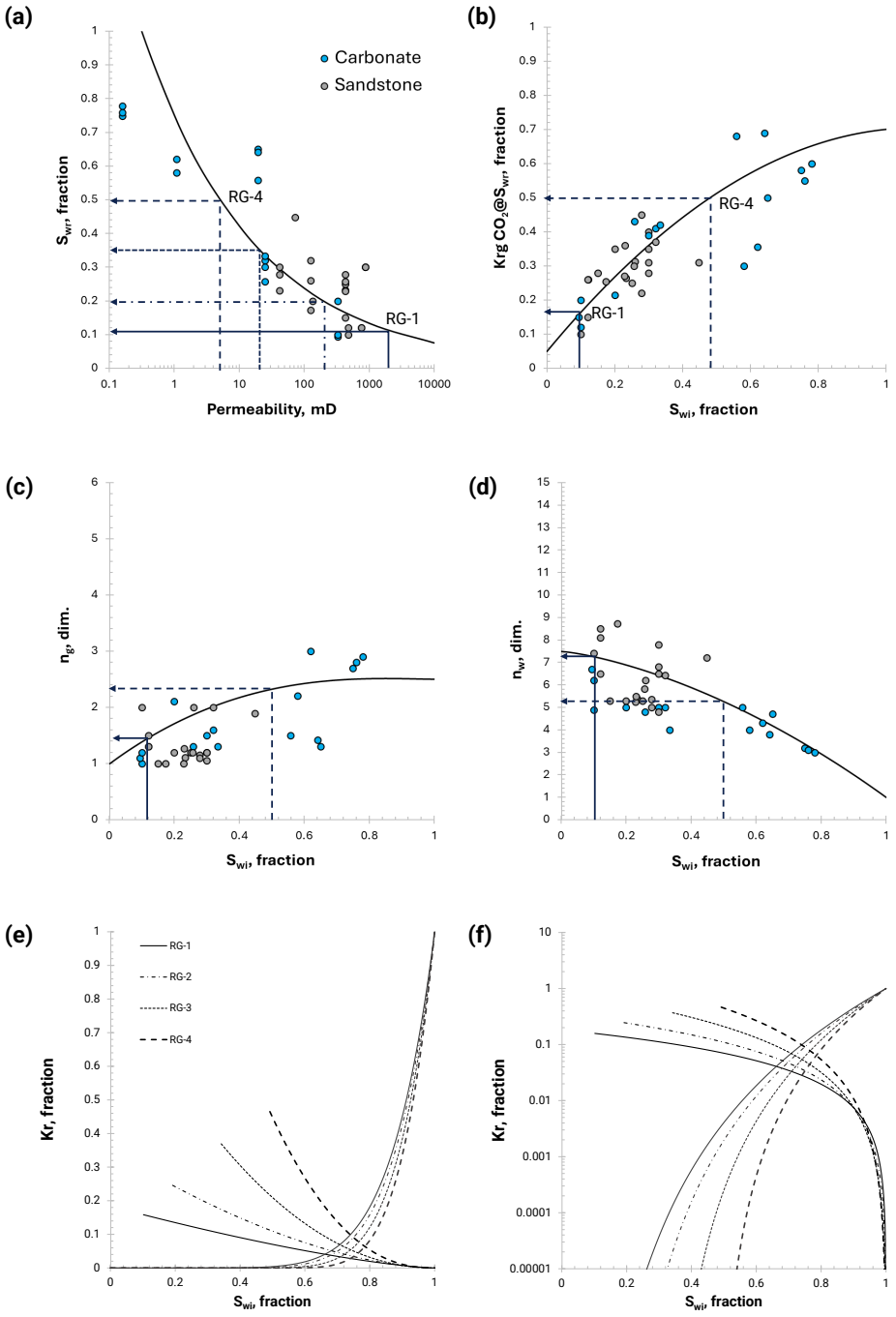



**Fig. 7** — Application of the SCAL trend model to predict primary drainage $CO_2$–brine relative permeability curves for four rock groups (RG-1 to RG-4) defined by simple permeability classification, with each group spanning approximately one logarithmic cycle of permeability. Subfigures show: (a) $S_{wi}$ versus permeability with rock group assignments; (b) $CO_2$ endpoint relative permeability at $S_{wir}$; (c) $CO_2$ Corey exponent; (d) water Corey exponent; (e) predicted relative

permeability curves per rock group in linear scale; and (f) the same curves on a semi-log scale. This illustrates the flexibility of the SCAL framework to generate physically consistent relative permeability curves across different permeability classes and reservoir flow units from a single calibrated trend model. Adapted from Akbar et al. (2025).

While the permeability-log-cycle grouping shown here serves as a practical and accessible starting point, the SCAL model in this study is equally compatible with more commonly used reservoir rock typing methodologies such as hydraulic flow unit (HFU) approach (Amaefule et al., 1993; Corbett and Potter, 2004; Abbaszadeh et al., 1996), pore geometry structure (PGS) (Musu et al., 2026; Akbar et al., 2025a,b; Hakiki et al., 2024), rock fabrics (Jennings and Lucia, 2003) and lithofacies-based classification (Skalinski et al., 2006); and other rock typing methods. In all cases, the key input to the SCAL trend model remains the $S_{wi}$ assigned to each rock group, which can be derived directly from whichever classification scheme is adopted. The framework therefore scales naturally from simple permeability-based grouping to fully integrated petrophysical rock typing, without requiring dedicated coreflood experiments for each group.

This scalability substantially extends the practical value of the framework for field-scale CCS modeling. In full-field reservoir simulations where multiple flow units with contrasting petrophysical properties must be represented simultaneously, the ability to generate group-specific relative permeability curves from a single calibrated SCAL model offers a significant advantage over generic or deterministic curve assignment. Physical consistency is preserved across all rock groups because every curve shares the same underlying wettability-driven trend structure anchored to the same experimental dataset. The framework thus provides a fit-for-purpose and scalable solution for integrating SCAL uncertainty into CCS reservoir simulation workflows across diverse geological and operational settings.

### *Final Relative Permeability Curves for Reservoir Simulation*

Building on the SCAL-based parameter trends and representative relative permeability curves illustrated in Figures 3e–f and 4e–f, a reference reservoir permeability of 100 mD is selected to define the final drainage and imbibition relative permeability models used in reservoir simulation. This permeability represents an intermediate flow regime within the compiled dataset and provides a consistent and practical basis for assessing the impact of relative permeability uncertainty on $CO_2$ storage performance.

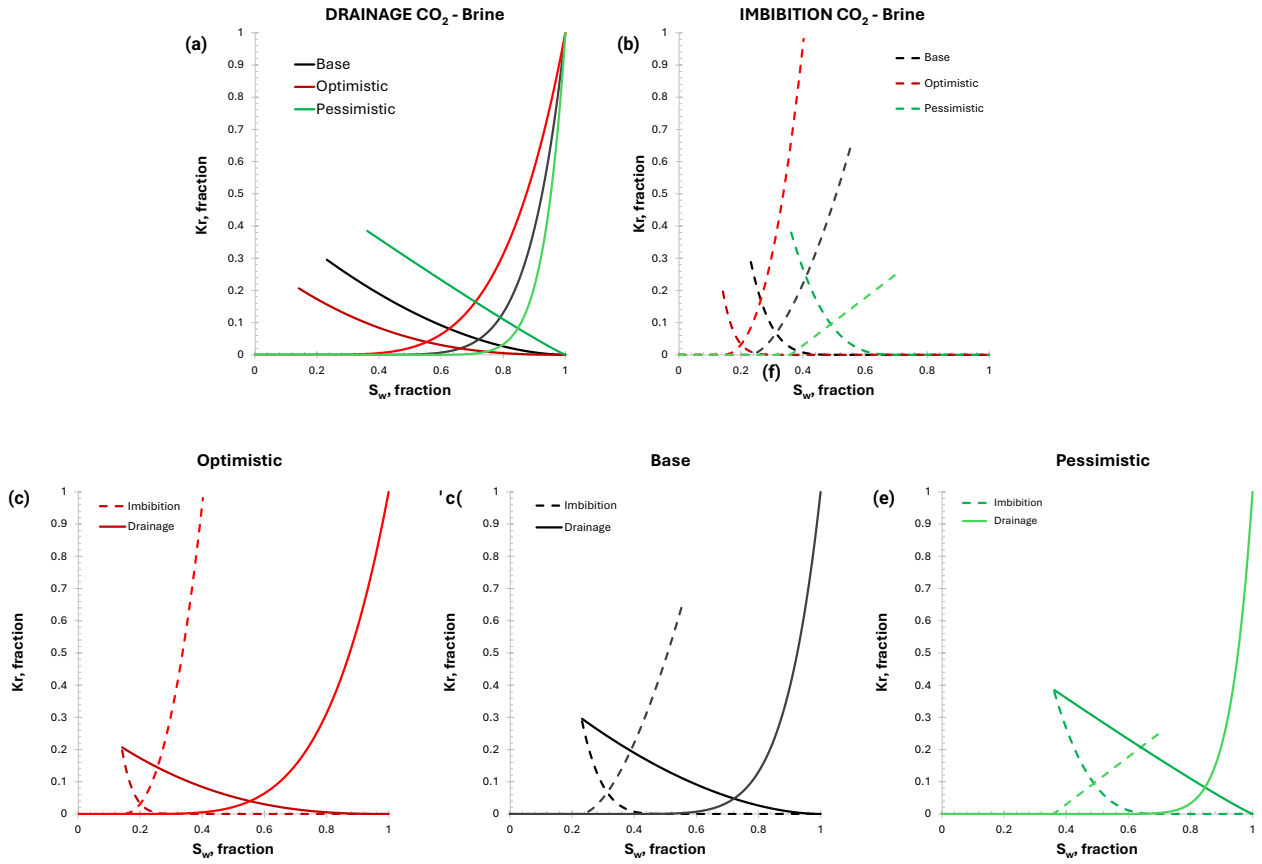



**Fig. 8** — Final relative permeability models derived from SCAL-based uncertainty modeling and used as input to reservoir simulations. Subfigures (a) and (b) show the uncertainty-bounded primary drainage and imbibition $CO_2$–brine relative permeability envelopes. Subfigures (c)–(e) present paired drainage and imbibition curves for the optimistic, base-case, and pessimistic scenarios, illustrating contrasts in $CO_2$ mobility, phase hysteresis, and trapping potential.

Figure 8 summarizes the final set of $CO_2$–brine relative permeability curves derived from the SCAL-based uncertainty modeling workflow. Figures 8a and 8b present the uncertainty-bounded primary drainage and imbibition envelopes, while Figures 8c–8e present the paired drainage and imbibition curves for each uncertainty scenario, emphasizing the contrasts in multiphase flow behavior between injection and post-injection conditions. In the optimistic model, reduced $CO_2$ relative permeability during drainage and stronger $CO_2$ immobilization during imbibition result in limited gas-phase mobility, leading to slower plume advance and enhanced long-term trapping. In contrast, the pessimistic model exhibits higher $CO_2$ mobility during both drainage and imbibition, promoting faster plume migration and reduced containment despite improved injectivity. These final relative permeability models constitute the primary link between laboratory-scale SCAL uncertainty and reservoir-scale performance assessment.

## RESERVOIR SIMULATION FRAMEWORK AND RESULTS

### *Model Description*

The static and dynamic reservoir models were built using the integrated reservoir simulation software tNavigator. Simulations were performed using a compositional formulation with CO2STORE keywords to represent $CO_2$ dissolution into the brine phase. A synthetic aquifer model was constructed as a two-dimensional vertical cross-section (X–Z plane) with a single grid cell in the Y-direction, enabling focused investigation of buoyancy-driven plume migration, injectivity behavior, and long-term trapping mechanisms without confounding effects from geological heterogeneity.

The model represents a reservoir domain approximately 2.4 km wide and 97 m thick. The effective simulation grid resolution is approximately 20 m in the horizontal direction and 1 m in the vertical direction, providing sufficient vertical refinement to capture gravity segregation, capillary trapping, and post-injection saturation redistribution. The reservoir is assumed to be laterally homogeneous, with uniform porosity and permeability throughout the domain. This simplified representation is intentionally adopted to isolate the impact of relative permeability uncertainty—particularly drainage–imbibition hysteresis—on $CO_2$ plume evolution and trapping, without interference from geological complexity.

Initial reservoir pressure and temperature are set to 200 bar and 100 °C, respectively, ensuring that injected $CO_2$ remains in a supercritical state throughout the simulation period. The reservoir is initially fully saturated with brine at a salinity of 10,000 ppm. Capillary pressure is held constant across all simulation cases so that differences in plume behavior and trapping efficiency arise solely from variations in relative permeability. $CO_2$ is injected as a pure component through a single vertical injection well at a rate-controlled injection of 100,000 $m^3$/day for a period of 2 years, followed by a 1,000-year post-injection simulation period. Boundary conditions represent an open aquifer system, allowing pressure dissipation during and after injection.

### *$CO_2$ Plume Evolution*

$CO_2$ plume evolution is a critical determinant of storage performance, as it governs the spatial extent of $CO_2$ migration, pressure distribution, and the effectiveness of trapping mechanisms over time. Understanding how relative permeability uncertainty influences plume behavior is therefore essential for assessing containment security and long-term storage risk.

Figure 9 illustrates the evolution of the $CO_2$ plume for the optimistic, base-case, and pessimistic relative permeability scenarios at the end of injection (2 years) and during the post-injection period (300 and 1,000 years). Clear differences in plume geometry, lateral migration, and long-term gas-phase mobility are observed across the three scenarios, demonstrating the first-order control exerted by relative permeability uncertainty on $CO_2$ plume evolution.

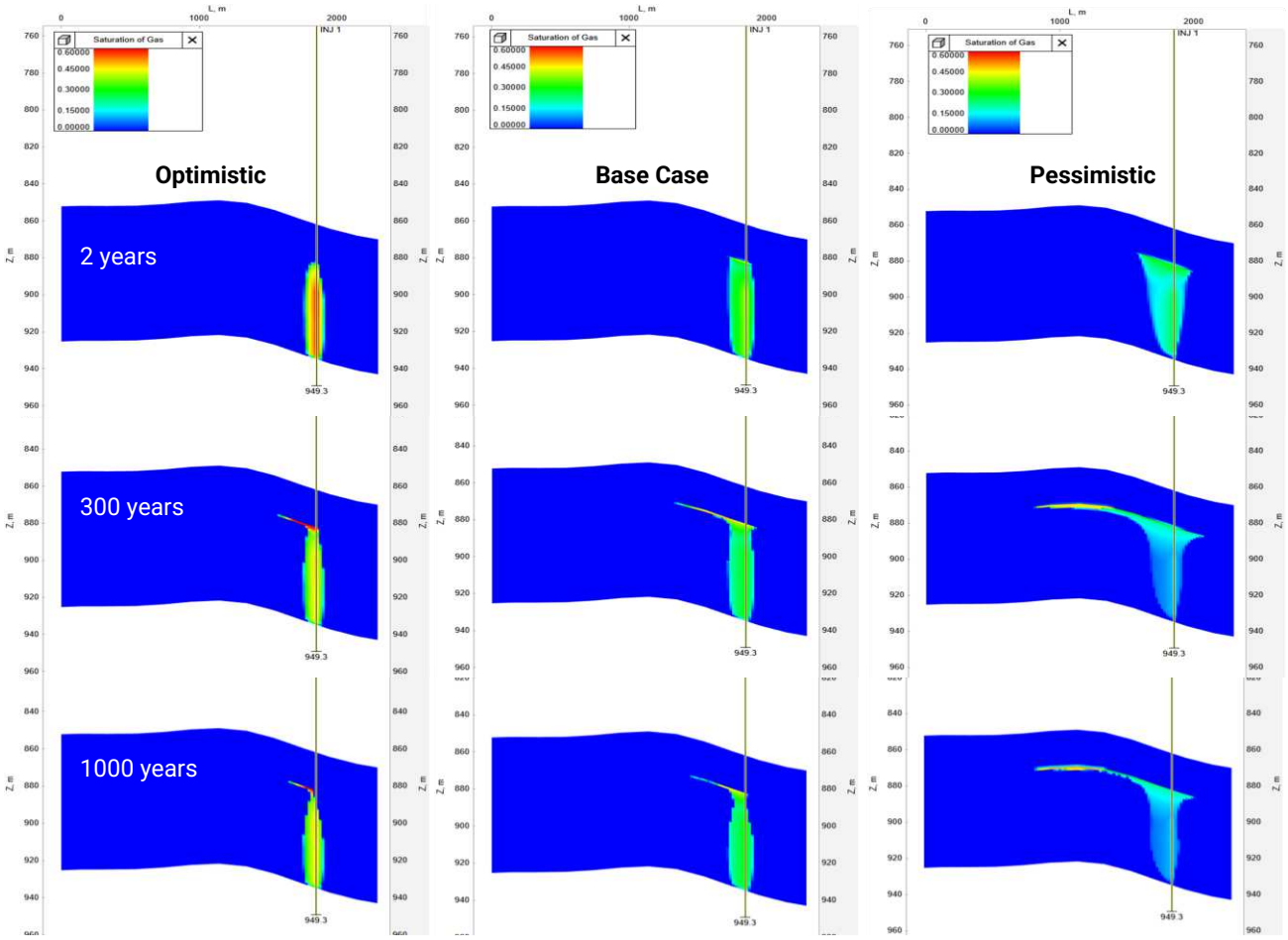



**Fig. 9** — Spatial distribution of $CO_2$ free gas saturation for optimistic, base-case, and pessimistic relative permeability scenarios at the end of injection (2 years) and during post-injection periods (300 and 1,000 years). Differences in plume geometry, lateral migration, and long-term gas-phase mobility illustrate the sensitivity of $CO_2$ plume evolution to relative permeability uncertainty.

In the pessimistic case, high $CO_2$ endpoint relative permeability and higher irreducible water saturation result in elevated $CO_2$ mobility during injection. The plume exhibits rapid vertical segregation and pronounced lateral spreading shortly after injection commences. Even after 1,000 years, a laterally extensive plume with a significant mobile gas fraction persists, indicating sustained $CO_2$ mobility and delayed stabilization. A larger fraction of free $CO_2$ implies greater potential for long-range migration

and reduced containment security, as only immobilized (residual or dissolved) $CO_2$ contributes to long-term storage integrity.

The base-case scenario shows intermediate plume behavior. $CO_2$ migration is slower and more compact than in the pessimistic case, while still maintaining sufficient injectivity. Over time, the plume gradually stabilizes as gas mobility decreases following injection shut-in, resulting in moderate lateral spreading and partial immobilization.

In contrast, the optimistic scenario produces a markedly more compact $CO_2$ plume. Reduced $CO_2$ mobility during primary drainage limits plume advance during injection, leading to reduced lateral extent and delayed vertical segregation. After injection shut-in, the plume stabilizes rapidly, and free gas saturation diminishes significantly over time. By 1,000 years, the mobile $CO_2$ footprint is considerably smaller compared with the other cases, reflecting enhanced containment associated with conservative relative permeability assumptions. This behavior is favorable for storage security, as a smaller fraction of $CO_2$ remains in a mobile (free-phase) state and a larger proportion is immobilized through residual and solubility trapping.

***$CO_2$ Dissolution and Solubility Trapping***

$CO_2$ dissolution and solubility trapping are critical for long-term storage security in geological $CO_2$ storage systems, as they progressively transfer $CO_2$ from a mobile free phase into the aqueous phase, reducing buoyancy forces and limiting the potential for large-scale plume migration and leakage. Understanding how relative permeability uncertainty influences $CO_2$–brine contact and dissolution behavior is therefore essential for reliable prediction of storage performance.

Figure 10 illustrates the evolution of brine mass density as a proxy for $CO_2$ dissolution and solubility trapping for the optimistic, base-case, and pessimistic relative permeability scenarios during injection and over the post-injection period. Differences in the magnitude and spatial extent of density enhancement across the scenarios highlight the sensitivity of solubility trapping to relative permeability-controlled plume migration and $CO_2$–brine contact.

In the optimistic case, sustained $CO_2$–brine contact resulting from slower plume migration leads to pronounced increases in brine density beneath the injector and along the plume margins. Dissolution progresses steadily over time, resulting in a broad zone of $CO_2$-enriched brine after 1,000 years, reflecting enhanced solubility trapping driven by prolonged residence time and reduced gas-phase

mobility. The base-case scenario exhibits moderate solubility trapping, with density increases confined to a narrower region beneath the plume. The pessimistic case shows more limited brine density enhancement: rapid plume migration and reduced $CO_2$–brine contact suppress dissolution, and dense brine zones remain localized even after 1,000 years, indicating a weaker contribution of solubility trapping to long-term storage security.

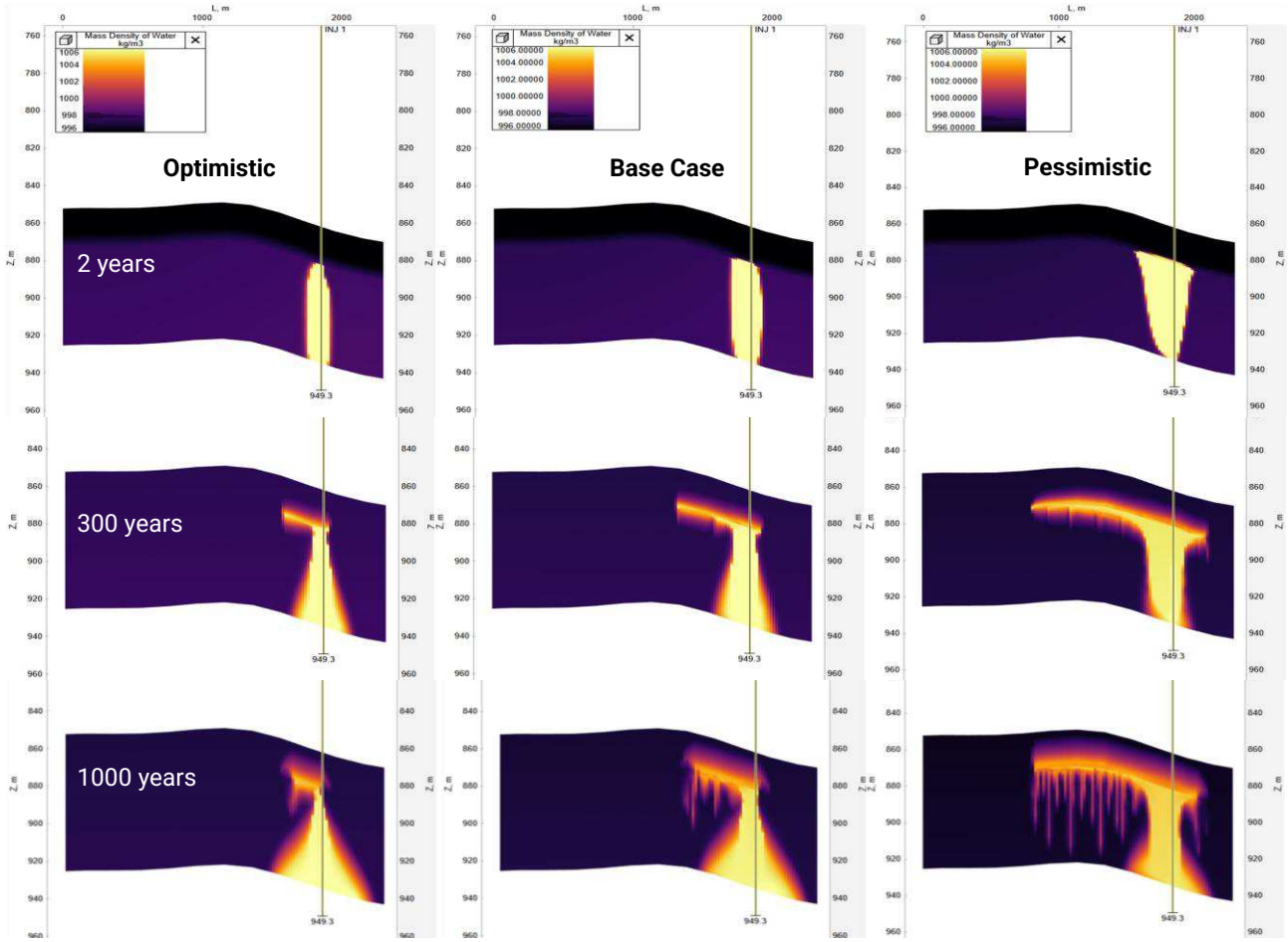



**Fig. 10** — Evolution of brine mass density for optimistic, base-case, and pessimistic relative permeability scenarios at 2, 300, and 1,000 years. Increased brine density indicates $CO_2$ dissolution into the aqueous phase, highlighting differences in solubility trapping efficiency and $CO_2$–brine contact associated with relative permeability uncertainty.

### *Evolution of $CO_2$ Trapping Mechanisms*

The evolution of $CO_2$ trapping mechanisms provides an integrated measure of storage performance by quantifying how injected $CO_2$ is redistributed over time among mobile, residually trapped, and dissolved phases. This redistribution is strongly influenced by relative permeability uncertainty and directly determines long-term storage security, as only immobile $CO_2$ contributes to permanent

containment. Figure 11 summarizes the temporal evolution of $CO_2$ trapping mechanisms over the full 1,000-year simulation period, distinguishing between mobile $CO_2$, residually trapped $CO_2$, and $CO_2$ dissolved in brine.

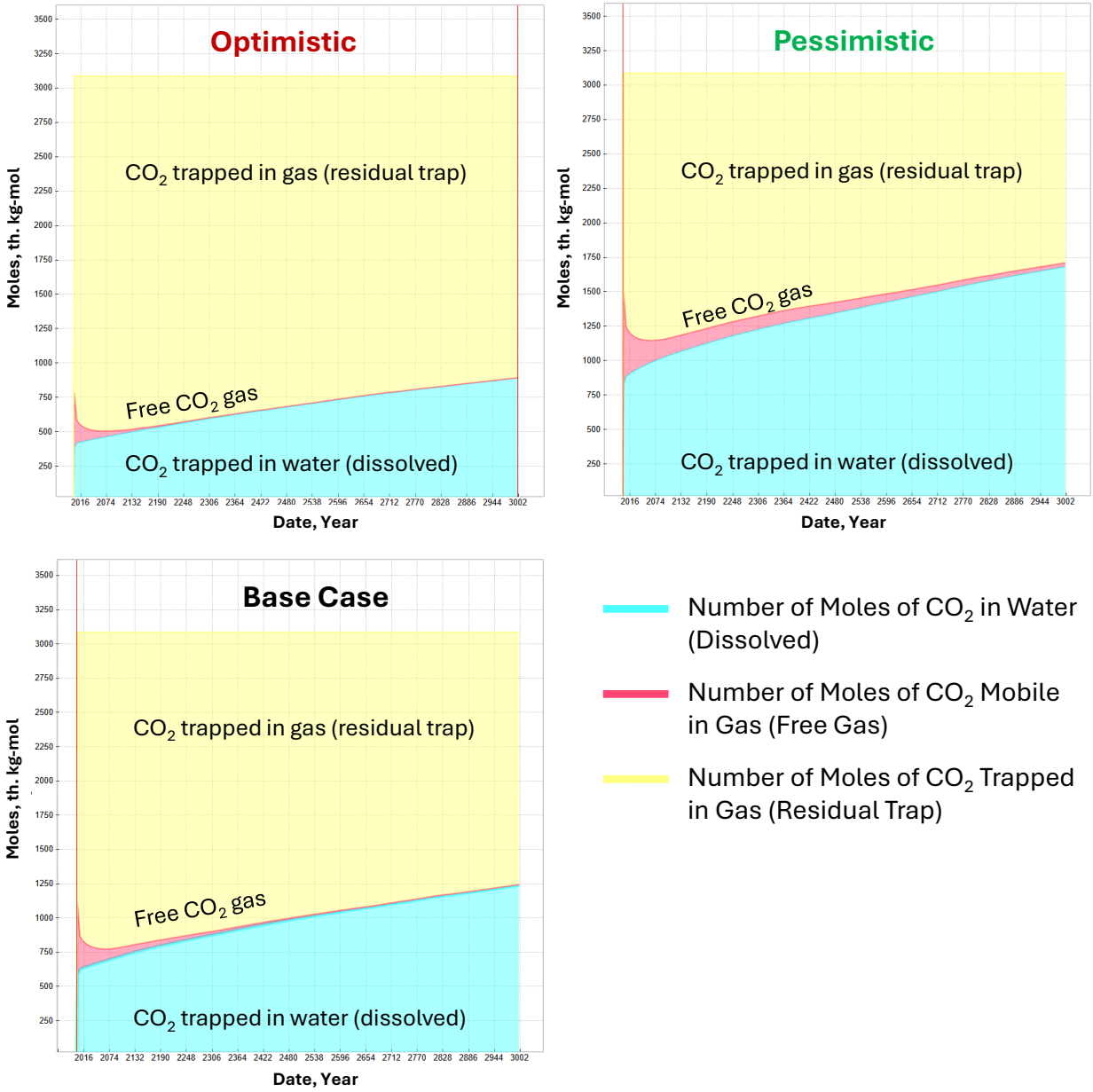



**Fig. 11** — Temporal evolution of $CO_2$ trapping mechanisms over a 1,000-year simulation period for optimistic, base-case, and pessimistic relative permeability scenarios. The relative contributions of mobile $CO_2$, residually trapped $CO_2$, and dissolved $CO_2$ illustrate the impact of drainage and imbibition relative permeability uncertainty on long-term storage security.

In the optimistic scenario, residual trapping becomes the dominant immobilization mechanism shortly after injection shut-in. High residual gas saturation during imbibition results in rapid conversion of

free $CO_2$ gas into trapped ganglia. Over time, solubility trapping increases steadily, further reducing the mobile $CO_2$ fraction. By the end of the simulation period, only a small portion of the injected $CO_2$ remains mobile, indicating strong long-term containment.

The base-case scenario displays a balanced contribution from residual and solubility trapping. While a substantial fraction of $CO_2$ becomes immobilized, the decline in mobile gas occurs more gradually, reflecting intermediate imbibition behavior and partial gas connectivity during early post-injection times.

The pessimistic scenario retains the largest mobile $CO_2$ fraction throughout the simulation period. Lower residual gas saturation and weaker capillary trapping allow a significant portion of $CO_2$ to remain mobile long after injection ceases. Although dissolution continues to increase over time, it does not fully compensate for the limited residual trapping, resulting in a storage outcome dominated by prolonged gas-phase mobility.

Although the total injected $CO_2$ inventory is essentially the same in all scenarios (approximately 3065 thousand kg-mol), Figure 11 shows that relative permeability uncertainty exerts a strong control on how this mass is redistributed over time among mobile, residually trapped, and dissolved $CO_2$. The principal difference between the scenarios therefore lies not in the amount of $CO_2$ injected, but in the rate and extent to which the injected inventory is transferred from a mobile gas phase into more secure trapping states after injection shut-in. In the optimistic case, this redistribution occurs rapidly, with residual trapping dominating early and dissolution increasing progressively thereafter. In contrast, the pessimistic case retains a substantially larger mobile fraction for a much longer period, reflecting delayed immobilization and greater long-term migration potential. The base-case scenario exhibits intermediate behavior between these two end members. This comparison highlights that relative permeability uncertainty governs not only plume geometry and injectivity, but also the temporal partitioning of the injected $CO_2$ inventory and, consequently, the evolution of long-term storage security.

***Integrated Summary of Uncertainty Effects***

The integrated assessment of relative permeability uncertainty is essential for evaluating overall $CO_2$ storage performance, as it links multiphase flow behavior to key operational and long-term outcomes including injectivity, plume migration, trapping efficiency, and containment security. Synthesizing

these effects into a unified framework enables clearer interpretation of how uncertainty propagates through the system and informs CCS project design and risk assessment.

Table 2 provides a structured summary of how uncertainty in relative permeability parameters translates into differences in injectivity, $CO_2$ plume behavior, trapping efficiency, and long-term storage security, synthesizing the combined effects of primary drainage and imbibition behavior across the three uncertainty scenarios.

**Table 2** — Summary of the combined effects of primary drainage and imbibition relative permeability uncertainty on injectivity, $CO_2$ plume behavior, trapping efficiency, and long-term storage security for the optimistic, base-case, and pessimistic scenarios.

| Aspect | Optimistic | Base Case | Pessimistic |
|---|---|---|---|
| **$CO_2$ endpoint kr** | Low (reduced mobility) | Intermediate | High (elevated mobility) |
| **Swir** | Low | Intermediate | High |
| **Injectivity** | Moderately lower; higher BHP | Intermediate | Higher; lower BHP |
| **Plume geometry** | Compact, vertically confined | Intermediate lateral spread | Extensive lateral migration |
| **Residual trapping (Sgr)** | High | Intermediate | Low |
| **Solubility trapping** | Enhanced (prolonged $CO_2$–brine contact) | Moderate | Suppressed (limited contact) |
| **Long-term $CO_2$ mobility** | Low (rapid stabilization) | Moderate | High (sustained mobility) |
| **Storage security** | High | Intermediate | Lower |

Collectively, the simulation results demonstrate that relative permeability uncertainty introduces fundamental trade-offs between injectivity, plume control, trapping efficiency, and storage security. Differences in primary drainage behavior dictate plume extent and injectivity during injection, while imbibition parameters control the rate and effectiveness of post-injection plume immobilization. These competing effects imply that CCS system performance cannot be optimized by considering a single metric in isolation. Instead, robust storage design requires balancing injectivity and containment objectives under uncertainty. The optimistic, base-case, and pessimistic scenarios therefore represent fundamentally different risk–performance envelopes over 1,000-year timescales, underscoring the critical importance of explicitly accounting for relative permeability uncertainty in CCS decision-making.

## DISCUSSION

The results presented in this study demonstrate that $CO_2$–brine relative permeability uncertainty represents a first-order control on geological $CO_2$ storage performance, with implications that span the full lifecycle of a CCS project from injection operations to long-term containment. Several key insights emerge from the integrated SCAL-based uncertainty framework and reservoir simulation results.

First, the role of initial water saturation as an organizing variable extends beyond its traditional interpretation as a simple endpoint saturation. This study confirms that $S_{wi}$ implicitly encodes pore structural information—particularly pore throat size distribution, wettability, and capillary entry pressures—that governs both drainage and imbibition behavior in a physically correlated way. This means that uncertainty in $S_{wi}$ propagates coherently through all Corey parameters, producing scenarios that are internally consistent rather than independently randomized. This physical consistency is a key strength of the proposed framework over purely statistical uncertainty quantification approaches.

Second, the opposing effects of relative permeability uncertainty on injectivity versus trapping security represent a critical trade-off for CCS project design. Pessimistic relative permeability scenarios, which favor high $CO_2$ endpoint permeability and weak capillary trapping, produce excellent injectivity conditions but poor long-term containment. Optimistic scenarios show the reverse tendency. This trade-off cannot be resolved by optimizing a single parameter and must be considered holistically when selecting injection strategies, storage site targets, and monitoring approaches.

Third, the temporal dynamics of trapping mechanisms are strongly sensitive to relative permeability parameterization. Because residual trapping is established primarily in the period immediately following injection shut-in, imbibition parameters exert a disproportionate influence on the long-term fate of injected $CO_2$ despite acting over a narrower saturation range than drainage. This reinforces the necessity of treating drainage and imbibition as coupled components of a single uncertainty framework, rather than evaluating them separately.

The simplified reservoir geometry adopted in this study—homogeneous, laterally uniform, with constant capillary pressure—was intentionally designed to isolate the impact of relative permeability uncertainty from other sources of variability. In realistic storage systems, geological heterogeneity, capillary pressure variability, and structural trapping would interact with relative permeability effects and may either enhance or attenuate the sensitivities observed here. Future work should therefore extend this framework to heterogeneous reservoir models and evaluate the combined impact of geological and SCAL uncertainty on $CO_2$ storage performance and risk assessment.

## CONCLUSIONS

This study demonstrates that uncertainty in $CO_2$–brine relative permeability is a critical first-order control on long-term geological $CO_2$ storage performance. By integrating SCAL-based trend modeling, uncertainty-bounded relative permeability functions, and dynamic reservoir simulations, the workflow provides a systematic framework to evaluate how laboratory-scale variability propagates to reservoir-scale predictions. The principal conclusions are:

1. Initial water saturation ($S_{wi}$) serves as a physically meaningful organizing variable for both primary drainage and imbibition relative permeability behavior, capturing the combined effects of pore structure, wettability, and capillary-controlled displacement efficiency. By linking $S_{wi}$ to permeability and rock properties, the proposed framework enables generation of physically consistent relative permeability curves across different rock types or flow units without requiring dedicated SCAL measurements for each case. Variations in $S_{wi}$, together with uncertainty in endpoint relative permeabilities, Corey exponents, and residual gas saturation, lead to fundamentally different multiphase flow responses that cannot be represented by a single deterministic model.

2. Uncertainty in primary drainage relative permeability governs $CO_2$ mobility and plume migration during injection, while uncertainty in imbibition behavior controls post-injection plume stabilization through residual and solubility trapping. These processes are inherently coupled and must be treated within a unified framework.

3. Optimistic and pessimistic relative permeability scenarios produce fundamentally different storage outcomes. Reduced $CO_2$ mobility and higher residual gas saturation in the optimistic case result in compact plumes, enhanced trapping, and improved long-term containment, whereas higher mobility in the pessimistic case leads to faster plume migration, weaker trapping, and a larger fraction of mobile $CO_2$.

4. The SCAL-based framework developed in this study generates physically consistent uncertainty bounds rather than relying on deterministic or purely statistical representations, providing a transparent and defensible basis for CCS performance assessment under limited or unavailable experimental data. This makes the approach particularly suitable for early-stage screening and feasibility studies, where site-specific SCAL data are typically unavailable and relative permeability behavior must be inferred from analogue datasets.

5. The proposed workflow offers a practical approach for evaluating trade-offs between injectivity, plume control, trapping efficiency, and storage security, supporting more robust CCS design, risk assessment, and decision-making under uncertainty. Extension to heterogeneous systems and integration with geological uncertainty remain important directions for future work.

## ACKNOWLEDGEMENTS

The authors gratefully acknowledge Rock Flow Dynamics for providing access to the tNavigator software used in this study and for granting permission to publish the results. The authors also thank Dustin Crandall of the National Energy Technology Laboratory (NETL) for insightful discussions on coreflood data quality and for making the experimental data publicly accessible. Prores AS is acknowledged for supporting the coreflood simulation work and for providing the Sendra S-Core software used to reconcile relative permeability and capillary pressure data. Portions of this work were previously presented at the SPE Annual Technical Conference and Exhibition 2025 (SPE-227969-MS) and the SPE Europe Subsurface Conference 2026 (SPE-231936-MS). This journal manuscript represents a substantially extended and integrated contribution beyond those earlier conference publications.

## FUNDING

This research received no external funding.

## TRIAL REGISTRATION

Not applicable. This study is not a clinical trial.

## ETHICS, CONSENT TO PARTICIPATE, AND CONSENT TO PUBLISH

Not applicable.

## REFERENCES

Abbaszadeh, M., Fujii, H., and Fujimoto, F. 1996. Permeability prediction by hydraulic flow unit theory and applications. *SPE Formation Evaluation* 11(4): 263–271. https://doi.org/10.2118/30158-PA.

Akbar, M.N.A., Jenei, B., Ainesazi, S., Myhr, R., and Ganzer, L. 2025. $CO_2$–brine SCAL modeling: A data- and physics-driven approach to predict relative permeability and uncertainty for geological carbon storage. Paper SPE-227969-MS presented at the *SPE Annual Technical*

*Conference and Exhibition*, Houston, Texas, USA, October. https://doi.org/10.2118/227969-MS.

Akbar, M.N.A., Jenei, B., Lakos, M., Steffens, B., Kulaksiz, S., and Ganzer, L. 2026. Assessing the impact of relative permeability uncertainty on geological $CO_2$ storage using SCAL modeling and numerical simulation. Paper SPE-231936-MS presented at the *SPE Europe Subsurface Conference*, Bergen, Norway, April. https://doi.org/10.2118/231936-MS.

Akbar, M.N.A. and Myhr, R. 2024. Dynamic reservoir rock typing for supercritical $CO_2$–brine systems in sandstone. Paper SPE-218449-MS presented at the *SPE Norway Subsurface Conference*, Bergen, Norway, April. https://doi.org/10.2118/218449-MS.

Akbar, M.N.A., Putra, A.P., and Reppert, M.G. 2025b. A versatile workflow of pore geometry structure rock typing and Corey parameter-based relative permeability trend modeling. *Petrophysics* 66(6). https://doi.org/10.30632/PJV66N6-2025a1.

Akbar, M.N.A., Reppert, M.G., and Putra, A.P. 2025a. Modeling oil saturation below a present-day free water level and its impact on reserves uncertainty: An integrated approach using logs, PGS rock typing, SCAL modeling, and saturation depth function. Paper SPWLA-2025-0077 presented at the *SPWLA 66th Annual Logging Symposium*, Dubai, UAE, May. https://doi.org/10.30632/SPWLA-2025-0077.

Akbarabadi, M. and Piri, M. 2013. Relative permeability hysteresis and capillary trapping characteristics of supercritical $CO_2$/brine systems: An experimental study at reservoir conditions. *Advances in Water Resources* 52: 190–206. https://doi.org/10.1016/j.advwatres.2012.06.014.

Amaefule, J.O., Altunbay, M., Tiab, D., Kersey, D.G., and Keelan, D.K. 1993. Enhanced reservoir description using core and log data to identify hydraulic flow units and predict permeability in uncored intervals/wells. Paper SPE-26436-MS presented at the *SPE Annual Technical Conference and Exhibition*, Houston, Texas, USA, 3–6 October. https://doi.org/10.2118/26436-MS.

Anderson, W.G. 1986a. Wettability literature survey—Part 1: Rock/oil/brine interactions and the effects of core handling on wettability. *Journal of Petroleum Technology* 38: 1125–1145. https://doi.org/10.2118/13932-PA.

Anderson, W.G. 1986b. Wettability literature survey—Part 2: Wettability measurement. *Journal of Petroleum Technology* 38: 1246–1262. https://doi.org/10.2118/13933-PA.

Anderson, W.G. 1987a. Wettability literature survey—Part 5: The effects of wettability on relative permeability. *Journal of Petroleum Technology* 39(11): 1453–1468. https://doi.org/10.2118/16323-PA.

Anderson, W.G. 1987b. Wettability literature survey—Part 6: The effects of wettability on waterflooding. *Journal of Petroleum Technology* 39: 1605–1622. https://doi.org/10.2118/16471-PA

Bachu, S. 2008. $CO_2$ storage in geological media: Role, means, status, and barriers to deployment. *Progress in Energy and Combustion Science* 34(2): 254–273. https://doi.org/10.1016/j.pecs.2007.10.001.

Bachu, S. 2013. Drainage and imbibition $CO_2$/brine relative permeability curves at in situ conditions for sandstone formations in western Canada. *Energy Procedia* 37: 4428–4436. https://doi.org/10.1016/j.egypro.2013.07.001

Bachu, S. and Adams, J.J. 2003. Sequestration of $CO_2$ in geological media in response to climate change: Capacity of deep saline aquifers to sequester $CO_2$ in solution. *Energy Conversion and Management* 44(20): 3151–3175. https://doi.org/10.1016/S0196-8904(03)00101-8.

Bennion, D.B. and Bachu, S. 2008. Drainage and imbibition relative permeability relationships for supercritical $CO_2$/brine and $H_2S$/brine systems in intergranular sandstone, carbonate, shale, and anhydrite rocks. *SPE Reservoir Evaluation & Engineering* 11(3): 487–496. https://doi.org/10.2118/99326-PA.

Bennion, D.B. and Bachu, S. 2010. Drainage and imbibition $CO_2$/brine relative permeability curves at reservoir conditions for carbonate formations. Paper SPE-134028-MS presented at the *SPE Annual Technical Conference and Exhibition*, Florence, Italy. https://doi.org/10.2118/134028-MS.

Benson, S.M. and Cole, D.R. 2008. $CO_2$ sequestration in deep sedimentary formations. *Elements* 4(5): 325–331. https://doi.org/10.2113/gselements.4.5.325.

Class, H., Ebigbo, A., Helmig, R., Dahle, H.K., Nordbotten, J.M., Celia, M.A., Hassanizadeh, S.M., and Flemisch, B. 2009. A benchmark study on problems related to $CO_2$ storage in geologic formations. *Computational Geosciences* 13(4): 409–434. https://doi.org/10.1007/s10596-009-9146-x.

Corbett, P.W.M. and Potter, D.K. 2004. Petrotyping: A basemap and atlas for navigating through permeability and porosity data for reservoir comparison and permeability prediction. Paper presented at the *International Symposium of the Society of Core Analysts*, Abu Dhabi, UAE, 5–9 October. http://www.jgmaas.com/SCA/2004/SCA2004-30.pdf.

Corey, A.T. 1954. The interrelation between gas and oil relative permeabilities. *Producers Monthly* 19(1): 38–41.

Crandall, D., Moore, J., Brown, S., and King, S. 2019. *NETL–$CO_2$BRA relative permeability database*. National Energy Technology Laboratory, Morgantown, West Virginia. https://edx.netl.doe.gov/edxapps/co2bra

Ebeltoft, E., Lomeland, F., Brautaset, A., and Haugen, Å. 2014. Parameter-based SCAL—Analyzing relative permeability for full-field application. Paper presented at the *International Symposium of the Society of Core Analysts*, Avignon, France. https://jgmaas.com/SCA/2014/SCA2014-080.pdf

Hakiki, F., Akbar, M.N.A., and Muttaqin, Z. 2024. On the pore geometry and structure rock typing. *ACS Omega* 9(32): 34636–34649. https://doi.org/10.1021/acsomega.4c02879.

Jennings, J.W., Jr. and Lucia, F.J. 2003. Predicting permeability from well logs in carbonates with a link to geology for interwell permeability mapping. *SPE Reservoir Evaluation & Engineering* 6(4): 215–225. https://doi.org/10.2118/84942-PA.

Juanes, R., Spiteri, E.J., Orr, F.M., and Blunt, M.J. 2006. Impact of relative permeability hysteresis on geological $CO_2$ storage. *Water Resources Research* 42(12): W12418. https://doi.org/10.1029/2005WR004806.

Kianinejad, A., Chen, X., and DiCarlo, D.A. 2016. Direct measurement of relative permeability in rocks from unsteady-state saturation profiles. *Advances in Water Resources* 94: 1–10. https://doi.org/10.1016/j.advwatres.2016.04.018.

Krevor, S., Blunt, M.J., Benson, S.M., Pentland, C., Reynolds, C., Al-Menhali, A., and Niu, B. 2015. Capillary trapping for geologic carbon dioxide storage: From pore-scale physics to field-scale implications. *International Journal of Greenhouse Gas Control* 40: 221–237. https://doi.org/10.1016/j.ijggc.2015.04.006

Krevor, S., Pini, R., Zuo, L., and Benson, S.M. 2012. Relative permeability and trapping of $CO_2$ and water in sandstone rocks at reservoir conditions. *Water Resources Research* 48: W02532. https://doi.org/10.1029/2011WR010859.

Land, C.S. 1968. Calculation of imbibition relative permeability for two- and three-phase flow from rock properties. *Society of Petroleum Engineers Journal* 8(2): 149–156. https://doi.org/10.2118/1942-PA.

Mathias, S.A., Gluyas, J.G., Gonzalez, G.J., de Miguel, M., Bryant, S.L., and Wilson, D. 2013. On relative permeability data uncertainty and $CO_2$ injectivity estimation for brine aquifers. *International Journal of Greenhouse Gas Control* 12: 200–212. https://doi.org/10.1016/j.ijggc.2012.09.017.

Müller, N. 2011. Supercritical $CO_2$–brine relative permeability experiments in reservoir rocks—Literature review and recommendations. *Transport in Porous Media* 87(2): 367–383. https://doi.org/10.1007/s11242-010-9689-2.

Musu, J.T., Akbar, M.N.A., Permadi, P., and Widarsono, B. 2026. A novel type curve for sandstone rock typing. *Petrophysics* 67(1): 140–159. https://doi.org/10.30632/PJV67N1-2026a10.

Pini, R. and Benson, S.M. 2017. Capillary pressure heterogeneity and hysteresis for the supercritical $CO_2$/water system in a sandstone. *Advances in Water Resources* 108: 277–292. https://doi.org/10.1016/j.advwatres.2017.08.011.

Skalinski, M., Gottlib-Zeh, S., and Moss, B. 2006. Defining and predicting rock types in carbonates—Preliminary results from an integrated approach using core and log data from the Tengiz Field. *Petrophysics—SPWLA Journal of Formation Evaluation and Reservoir Description* 47(1).

Spiteri, E.J., Juanes, R., Blunt, M.J., and Orr, F.M. 2008. A new model of trapping and relative permeability hysteresis for all wettability characteristics. *SPE Journal* 13(3): 277–288. https://doi.org/10.2118/96448-PA.

Wang, D., Zheng, Z., Ma, Q., Hu, P., Huang, X., and Song, Y. 2020. Effects of the errors between core heterogeneity and the simplified models on numerical modeling of $CO_2$/water core flooding. *International Journal of Heat and Mass Transfer* 149: 119223. https://doi.org/10.1016/j.ijheatmasstransfer.2019.119223.